INTERNATIONAL JOURNAL FOR NUMERICAL METHODS IN FLUIDS, VOL. 14, 707–727 (1992)

SPECTRAL ELEMENT–FCT METHOD FOR SCALAR HYPERBOLIC CONSERVATION LAWS

JOHN GIANNAKOUROS AND GEORGE EM KARNIADAKIS*

Mechanical and Aerospace Engineering, Program in Applied and Computational Mathematics, Princeton University, Princeton, NJ 08544, U.S.A.

SUMMARY

A new algorithm based on spectral element discretizations and flux-corrected transport (FCT) ideas is developed for the solution of discontinuous hyperbolic problems. A conservative formulation is proposed, based on cell averaging and reconstruction procedures, that employs a staggered grid of Gauss–Chebyshev and Gauss–Lobatto–Chebyshev discretizations. In addition, high-order time-differencing schemes, a flux limiter and a general spectral filter are employed to improve the quality of the solution. It is demonstrated through model problems of linear advection and examples of one-dimensional shock formation that the proposed algorithm leads to stable, non-oscillatory solutions of high accuracy away from discontinuities. Typically, spectral or spectral element methods perform very poorly in the presence of even weak discontinuities, although they produce only exponentialy small errors for smooth solutions. Spectral element–FCT methods can provide spectral properties (i.e. minimum dispersion and diffusion errors) as well as great flexibility in the discretization, since a variable number of macroelements or collocation points per element can be employed to accommodate both accuracy and geometric requirements.

KEY WORDS Spectral element Flux-corrected transport Shock capturing Huperbolic discontinuous problems

1. INTRODUCTION

Spectral element methods are high-order weighted residual techniques for the solution of partial differential equations typically encountered in fluid dynamics.[1, 2] Their success in the recent past in simulating complex flows derives from the flexibility of the method in representing accurately non-trivial geometries while preserving the good resolution properties of spectral methods.[3] In these simulations, however, both the geometry and the solution are described through smooth functions, so that spectral element methods can obtain exponential accuracy by fully exploiting that regularity. There are numerous fluid dynamics applications, however, where either very steep gradients or even jump discontinuities are present, e.g. interfaces in multiphase flows, flame fronts or shocks in compressible flows. A straightforward application of high-order numerical methods in these situations is not possible, since large errors induced by the discontinuity (the Gibbs phenomenon) in addition to the standard dispersive and aliasing errors encountered in smooth solutions propagate in the domain and eventually render the solution with oscillations everywhere.

To demonstrate the Gibbs phenomenon in the spectral element discretization, we consider a Chebyshev approximation of the sign function (Figures 1(a)–1(c)). We see that indeed the

* Author to whom all correspondence should be addressed.

0271–2091/92/060707–21$10.50

Received 1 November 1990
Revised 21 June 1991

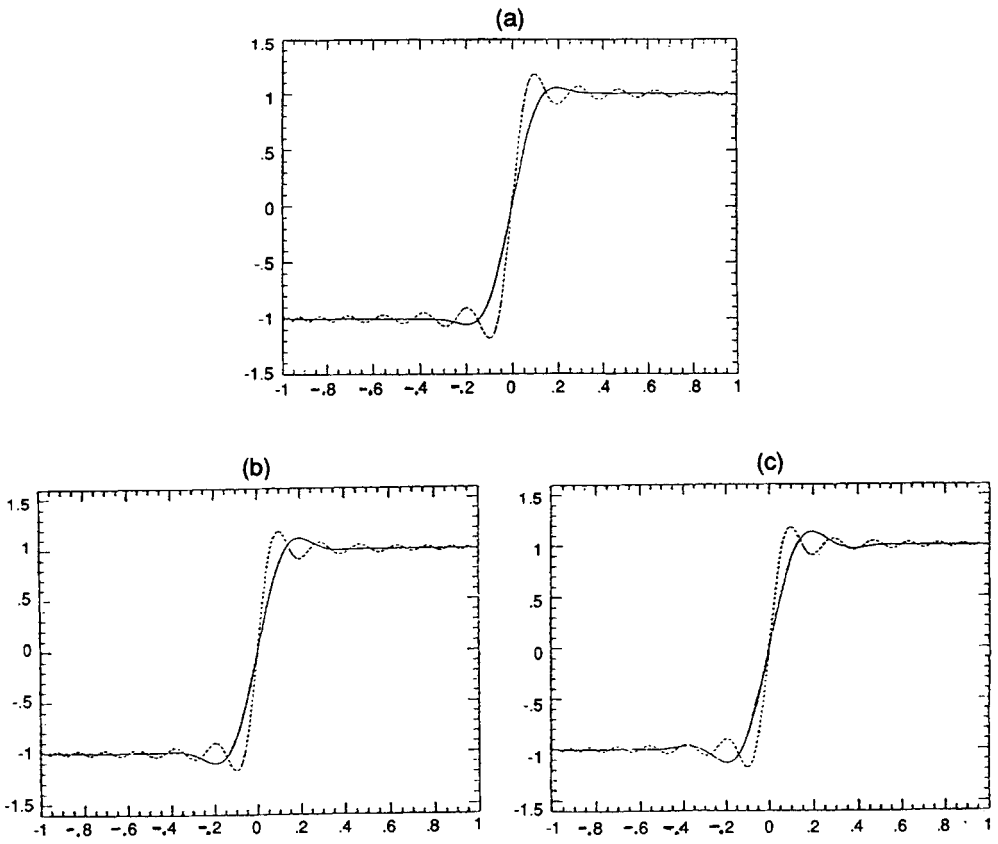

Figure 1. Spectral (Chebyshev) approximation of the sign function using $N = 32$ modes (dashed line). Solid lines represent the filtered solution using the Vandeven filter of order p: (a) $p = 3$; (b) $p = 6$; (c) $p = 10$

solution is inaccurate everywhere and that an increase in resolution does not improve the approximation. Incorporation of a high-order spectral (linear) filter developed by Vandeven[4] (see Section 5.3, equation (28)) improves the solution away from the discontinuity so that a prespecified accuracy is obtained according to the order of the filter, however, the solution in the neighbourhood of the discontinuity is still misrepresented, with the unfortunate occurrence that the width of the affected area increases with the filter order (Figures 1(b) and 1(c)). The latter is certainly an unwanted result in simulating phenomena where most of the physics stems from the discontinuous interface, as for example in the case of compressible flow in the presence of a shock wave. As a second example we consider the linear advection of a square wave in a periodic domain. In Figure 2 we plot a spectral element solution based on Chebyshev collocation after 750 000 time steps ($\Delta t = 10^{-3}$). There are two important features characteristic of this spectral element simulation: first, large-amplitude oscillations appear everywhere in the domain; secondly, the spectral element solution has been convected with the *correct phase speed* even after this very large number of time steps. While the second feature is indicative of the very small dispersion error of the method, the first feature is consistent with the argument made by Lax[5] that information is contained in these oscillations and that high-order schemes retain more information than low-order schemes.

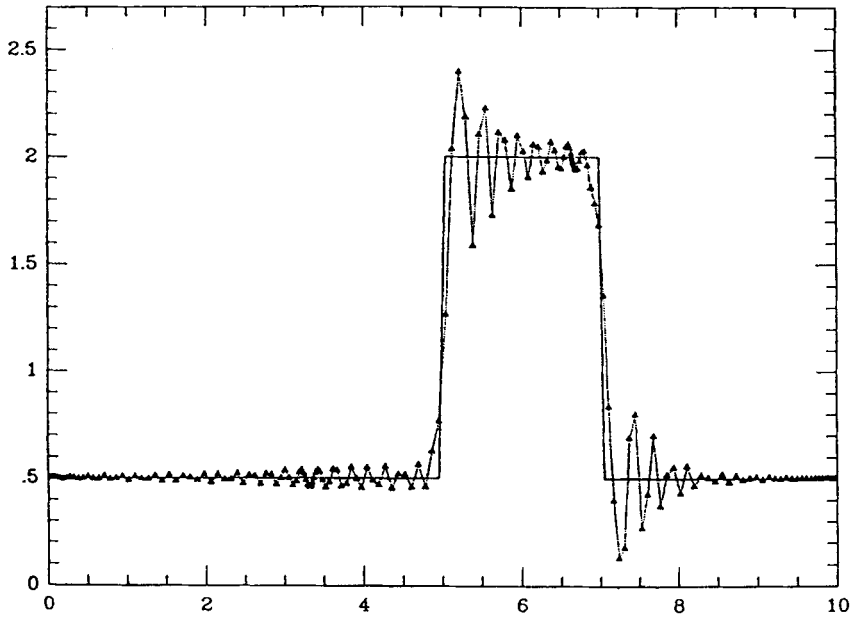

Figure 2. Linear advection of a square wave using spectral element discretizations ($K=3$, $N=60$). Periodic boundary conditions are imposed, while the time integration proceeds for 750 000 time steps of size $\Delta t = 10^{-3}$

One approach to successfully simulating the aforementioned complex flows is to use a non-linear, monotone, positivity-preserving method that will eliminate the Gibbs phenomenon and produce physically accepted solutions. This idea was first proposed in the seminal work of Boris and Book,[6,7] where an advection equation was considered as a model problem in the form

$$\frac{\partial \phi}{\partial t} + \frac{\partial f(\phi)}{\partial x} = 0. \tag{1}$$

The FCT algorithm proposed by Boris and Book consists mainly of two stages, a transport- or convective-diffusive stage and an antidiffusive or corrective stage. An equivalent but more descriptive interpretation of the FCT algorithm given later by Zalesak[8] suggested that the fluxes to be included in equation (1) can be considered as non-linear weighted averages of fluxes that can be computed by two distinct discretization schemes corresponding to different properties: one of first order that preserves monotonicity (according to Godunov's theorem[9]) and the other of high order that corrects the solution and *dictates* the accuracy. This latter observation is what motivated Zalesak[10] to incorporate a 16th-order finite difference formula and a pseudospectral method as high-order discretization schemes in a finite volume discretization method. More recently McDonald[11] has also studied the pseudospectral method as part of an FCT algorithm in solving scalar hyperbolic equations; in particular, he demonstrated through numerical experimentation the superiority in accuracy regarding phase and group velocities as compared to finite difference schemes of all orders.

Although very accurate, the FCT–pseudospectral method described in these previous works is limited to periodic computational domains with highly regular nodal point distribution. In the current work we attempt to relax these constraints by substituting for the high-order scheme a spectral element method.[1,2] In the spectral element discretization the computational domain is

broken into several subdomains (macroelements) within which data and unknowns are represented as spectral expansions in terms of general eigenfunctions—solutions of the singular Sturm–Liouville problem, i.e. Chebyshev polynomials, Legendre polynomials, etc. The discrete equations are derived via variational statements, so that the unknowns at each node represent values of the unknown field variable. This approach and its variants[3, 12, 13] result in exponential (spectral-like) convergence for infinitely smooth solutions. Besides the accuracy, however, that the method provides, it is the flexibility in the discretization and its easy extension in multidimensions that make it a prime candidate in problems of compressible turbulence and complex geometry applications. The paper is organized as follows. In Section 2 we introduce the basic ideas upon which our conservative spectral element formulation is based (cell-averaging procedures). In Sections 3 and 4 the approximation considerations needed to construct the full combined scheme proposed here are put forward (reconstruction procedure). In Section 5 we briefly review the FCT algorithm and describe its components (low- and high-order schemes, limiter and filter). Finally, results are presented in Section 6, followed by a brief discussion in Section 7.

2. CELL AVERAGES

In the general case that we consider in this work the nodal points are distributed in a non-uniform manner and thus we need to define appropriate cell-averaged quantities. In particular, adopting the terminology explained in Figure 3(a) the cell-averaged scalar quantity $\bar{\phi}_j$ is given by

$$\bar{\phi}_j \equiv \bar{\phi}(x_j, t) = \frac{1}{x_{i^+} - x_{i^-}} \int_{x_{i^-}}^{x_{i^+}} \phi(x, t)\mathrm{d}x. \tag{2}$$

Given this definition, equation (1) can be integrated along a cell extending form i^- to i^+ as

$$\frac{\mathrm{d}\bar{\phi}_j}{\mathrm{d}t} + \frac{f(\phi_{i^+}) - f(\phi_{i^-})}{\Delta x_j} = 0, \tag{3a}$$

where we have also defined

$$\Delta x_j \equiv x_{i^+} - x_{i^-}. \tag{3b}$$

The above equation therefore suggests that the fluxes $f(\phi)$ should be evaluated at the ends of the cell using *de-averaged* (reconstructed) velocity values; this formulation leads to the conservative (or flux) form of the semidiscrete wave equation.

In the following we define cell-averaged quantities for three particular discretizations: spectral (Fourier) discretization, spectral (Chebyshev) discretizations and spectral element (Chebyshev) discretizations. Proceeding with the first case, we refer to Figure 3(b), where the set of points j at which cell-averaged quantities are defined are simply the midpoints of the cell. Using the definition (2), a spectral expansion of the form

$$\phi(x) = \sum_{k=-N}^{N} a_k \mathrm{e}^{\mathrm{i}kx} \tag{4a}$$

corresponds to the cell-averaged quantity

$$\bar{\phi}(x) = \sum_{k=-N}^{N} \bar{a}_k \mathrm{e}^{\mathrm{i}kx}, \tag{4b}$$

where $\bar{a}_k = \sigma_k a_k$ and the (Dirichlet) kernel σ_k is given by

$$\sigma_k = \frac{\sin(k\Delta x/2)}{k\Delta x/2}, \tag{4c}$$

with $\Delta x = \pi/N$. This formulation results in an identical Fourier–FCT method to that presented in Reference 11, where a more heuristic approach was followed in the derivation.

A Chebyshev spectral expansion corresponds to a non-uniform distribution of points with cells of variable size Δx_j. Following the formulation of Cai *et al.*,[14] we select the set of points j to be the Gauss–Chebyshev points (see Figure 3(c)) defined by

$$x_j = \cos[(j-\tfrac{1}{2})\Delta\theta], \qquad \Delta\theta = \pi/N, \quad 1 \leqslant j \leqslant N, \tag{5a}$$

while the end points i^+ and i^- of each cell are the Gauss–Lobatto points defined as

$$x_i = \cos(i\Delta\theta), \quad 0 \leqslant i \leqslant N. \tag{5b}$$

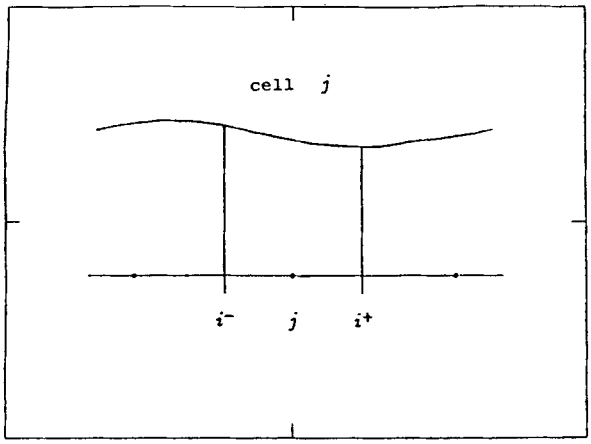

(a)

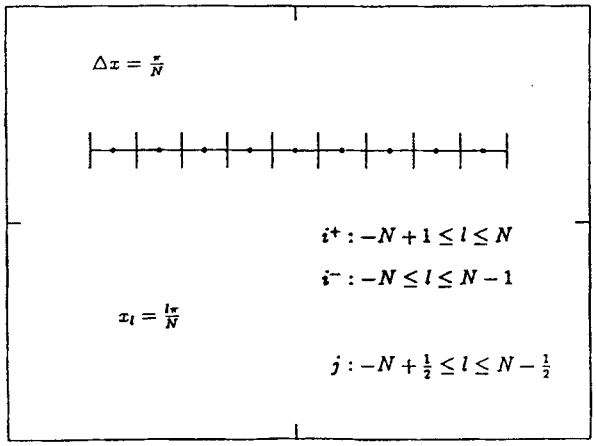

(b)

Figure 3. (Continued)

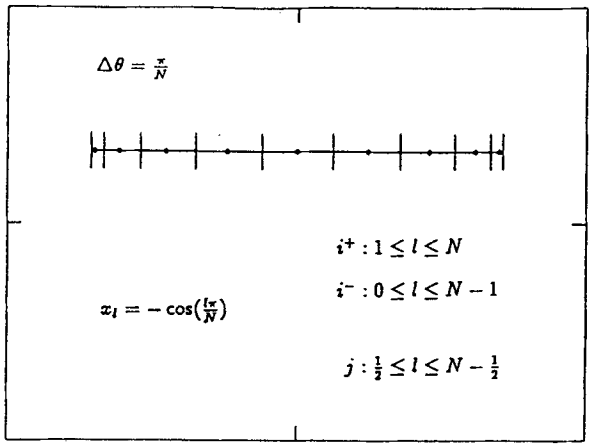

(c)

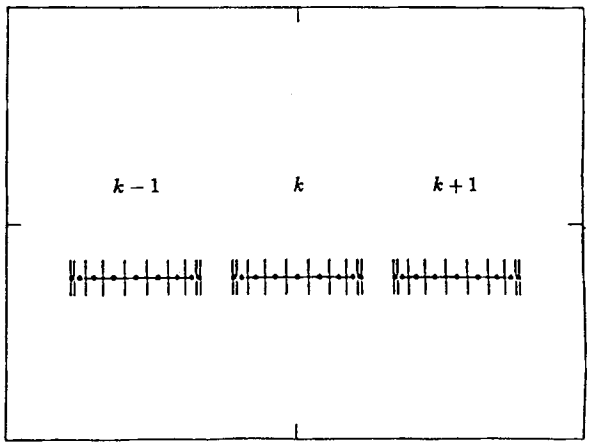

(d)

Figure 3. Definitions of (a) cell averages and (b)–(d) grids employed in discretizations: (b) Fourier; (c) Chebyshev; (d) spectral element. The set of points j define the cell-averaged quantities, while points i are used in evaluating the fluxes

Using these two sets of points and the definition (2), a Chebyshev spectral expansion of the form

$$\phi(x) = \sum_{k=0}^{N} a_k T_k(x) \tag{6a}$$

after averaging becomes

$$\bar{\phi}(x) = \sum_{k=0}^{N} a_k \bar{T}_k(x), \tag{6b}$$

where the cell-averaged Chebyshev polynomial is given by

$$\bar{T}_0 = 1, \tag{7a}$$

$$\bar{T}_1 = \tfrac{1}{2}\sigma_1 U_1(x), \tag{7b}$$

$$\bar{T}_k = \tfrac{1}{2}[\sigma_k U_k(x) - \sigma_{k-2} U_{k-2}(x)], \quad k \geqslant 2, \tag{7c}$$

with

$$\sigma_k = \frac{\sin[(k+1)\Delta\theta/2]}{(k+1)\sin(\Delta\theta/2)}. \tag{7d}$$

Here we have introduced $U_k(x) = [1/(k+1)]T'_{k+1}(x)$ to be the second kind of Chebyshev polynomials.

In the spectral element discretization the domain is broken up into several macroelements (Figure 3(d)) within which the velocity is expanded in terms of Chebyshev polynomials; C^0-continuity is imposed at the elemental boundaries. Therefore in the kth element an expansion of the form

$$\phi^k(x) = \sum_{i=0}^{N} \phi_i^k h_i(x), \tag{8a}$$

defined on the Gauss–Lobatto–Chebyshev points, after the application of the averaging operator takes the form

$$\bar{\phi}^k(x) = \sum_{i=0}^{N} \phi_i^k \bar{h}_i(x), \tag{8b}$$

where ϕ_i^k are the point values for element k; $h_i(x)$ and $\bar{h}_i(x)$ are the Gauss–Lobatto–Chebyshev–Lagrangian interpolant and its corresponding cell-averaged function obtained from

$$h_i(x) = \frac{2}{N} \sum_{p=0}^{N} \frac{1}{\bar{c}_i \bar{c}_p} T_p(x_i) T_p(x), \qquad 0 \leqslant i \leqslant N, \tag{9a}$$

$$\bar{h}_i(x) = \frac{2}{N} \sum_{p=0}^{N} \frac{1}{\bar{c}_i \bar{c}_p} T_p(x_i) \bar{T}_p(x), \qquad 0 \leqslant i \leqslant N, \tag{9b}$$

where $c_n = 1$ if $n \neq 0, N$ and $c_n = 2$ otherwise. In matrix form the above cell-averaging procedure can be written as

$$\bar{\phi}_j^k = A_{ji}^k \phi_i^k, \qquad 0 \leqslant i \leqslant N, \quad 0 \leqslant j \leqslant N, \tag{10}$$

where the cell-averaging matrix is defined as $A_{ji}^k = \bar{h}_i(x_j)$; here x_j refers to the local co-ordinate (see Section 5.2). On the basis of the nodal cell-averaged values obtained from (10), the corresponding polynomial can be constructed using Lagrangian interpolation, i.e.

$$\bar{u}(x) = \sum_{j=1}^{N} \bar{\phi}_j^k g_j(x), \tag{11a}$$

where the Gauss–Chebyshev–Lagrangian interpolant is given by

$$g_j(x) = (-1)^{j+1} \frac{1-x_j^2}{x_j} \frac{T_N(x)}{N}, \quad 1 \leqslant j \leqslant N. \tag{11b}$$

Having constructed a cell-averaging procedure for the spectral element discretization, we proceed next with the inverse operation of de-averaging and recovering point values for the evaluation of fluxes in equation (3a).

3. RECONSTRUCTION AND POINT VALUES

The reconstruction operation can also be put into matrix form. We consider first the polynomial describing the cell-averaged values,

$$\bar{\phi}(x)=\sum_{j=1}^{N}\bar{\phi}_j^k g_j(x). \tag{12a}$$

An alternative to expression (11b) for the Gauss–Chebyshev–Lagrangian interpolant is

$$g_j(x)=\sum_{p=0}^{N-1}\frac{2}{N\bar{c}_p}T_p(x_j)T_p(x). \tag{12b}$$

We can also express the $g_j(x)$ in terms of the second-kind Chebyshev polynomials; to this end we recall that[15]

$$T_p(x)=\tfrac{1}{2}[U_p(x)-U_{p-2}(x)], \quad p\geqslant 2. \tag{13a}$$

Using the above equation, we can rewrite $g_j(x)$ as

$$g_j(x)=\sum_{p=0}^{N-1}\lambda_p^j\sigma_p U_p(x), \quad 1\leqslant j\leqslant N. \tag{13b}$$

Here we have defined

$$\lambda_p^j=\frac{1}{N}T_p(x_j), \qquad p=N-2, N-1, \tag{13c}$$

$$\lambda_p^j=\frac{1}{N}[T_p(x_j)-T_{p+2}(x_j)], \qquad 0\leqslant p\leqslant N-3. \tag{13d}$$

The interpolating polynomial corresponding to point values (Gauss–Chebyshev–Lobatto points) can then constructed using the *de-averaged* Lagrangian interpolants G_j as

$$\phi(x)=\sum_{j=1}^{N}\bar{\phi}_j^k G_j(x). \tag{14}$$

The cell-averaged second-kind Chebysev polynomial is obtained using the definition of equation (2) (see details in Reference 14):

$$\bar{U}_p(x)=\sigma_p U_p(x), \tag{15}$$

with σ_p obtained from equation (7d). To determine $G_j(x)$, therefore, consider (14), (15) and (12a)–(13b) and obtain

$$G_j(x)=\sum_{p=0}^{N-1}\frac{\lambda_p^i}{\sigma_p}U_p(x). \tag{16}$$

To recover the point values u_i, we simply set $x=x_i$ in the interpolating polynomial $u(x)$. In matrix form the reconstruction procedure (on an elemental level) can be written in the form

$$\phi_i=g_{ij}^*\bar{\phi}_j, \quad 1\leqslant j\leqslant N, \quad 1\leqslant i\leqslant N, \tag{17a}$$

where

$$g_{ij}^{*} = G_j(x_i). \tag{17b}$$

On the basis of these N point values, the interpolating polynomial $\phi(x)$ can then be constructed from equation (14). This local reconstruction procedure is then repeated for all elements. To form a global interpolating polynomial, however, we need to impose a continuity condition at elemental interfaces as we explain in the next section.

4. INTERFACIAL CONSTRAINT

The interpolation polynomial $\phi(x)$ constructed on the basis of the Gauss–Lobatto–Chebyshev points is of degree N (requiring $N+1$ values to be determined), while we only obtain N point values from the reconstruction procedure (equation (17)). The additional information needed to uniquely define $\phi(x)$ comes from requiring continuity of solution at the interfacial nodal points. For the kth element, for example, we require that the rightmost nodal value be equal to the leftmost nodal value of element $k+1$, i.e. $\phi_0^{k+1} = \phi_N^k$ (Figure 3(d)). This can be accomplished by adding an extra term to the $(N-1)$th-order polynomial as follows:

$$\phi^{k+1}(r) = \sum_{j=1}^{N} \bar{\phi}_j^{k+1} G_j(r) + (1-r) T_N'(r) \frac{\delta\phi^k}{2N^2}, \tag{18a}$$

where the jump $\delta\phi^k$ is defined by

$$\delta\phi^k = \phi_N^k - \sum_{j=1}^{N} \bar{\phi}_j^{k+1} G_j(-1). \tag{18b}$$

Here the co-ordinate r refers to the local element co-ordinate and $(-1, 1)$ are the end points of the mapped element (see Section 5.2).

The above approach results in a formally discontinuous cell-averaged interpolating polynomial $\bar{\phi}(x)$ across elemental boundaries; however, the discontinuity can become spectrally small as the elemental resolution N increases. The implementation of Dirichlet boundary conditions is similar to the above imposition of the interfacial continuity constraint.

5. FCT ALGORITHM

To demonstrate the flux-corrected transport algorithm, we consider here the linearized form of equation (1) as follows:

$$\frac{\partial\phi}{\partial t} + U\frac{\partial\phi}{\partial x} = 0, \tag{19}$$

where U represents a convective velocity for the field $\phi(x, t)$. Here we adopt the approach of Zalesak[8] in formulating an FCT algorithm where a low-order solution denoted by $\bar{\phi}_j^{td}$ is computed first, followed by application of a flux-limiting procedure which leads to the final field $\bar{\phi}_j^{n+1}(x, t)$; here n refers to the level of time step up to which the solution is known.

In particular, the main steps of the proposed spectral element–FCT method are as follows.

(1) The initial condition $\phi(x, 0)$ is cell-averaged to obtain the field $\bar{\phi}_j(0)$ on the Gauss–Chebyshev mesh.

At time step $n\Delta t$:

(2) Compute the transportive flux f_i corresponding to a low-order scheme at each Gauss–Lobatto-Chebyshev nodal point.
(3) Advance (explicitly) the low-order transportive–diffusive solution to obtain $\bar{\phi}_j^{\mathrm{td}}$.
(4) Compute the transportive flux F_i corresponding to the spectral element discretization scheme; again the Gauss–Lobato–Chebyshev points are employed in the discretization.
(5) Compute and limit the antidiffusive flux A_i^{c}:

$$A_i^{\mathrm{c}} = C_i(F_i - f_i), \quad 0 \leqslant C_i \leqslant 1. \tag{20}$$

(6) Through reconstruction obtain de-averaged values ϕ_i.
(7) Update (explicitly) the final solution based on the limited antidiffusive fluxes, i.e.

$$\bar{\phi}_j^{n+1} = \bar{\phi}_j^{\mathrm{td}} - \frac{\Delta t}{\Delta x_j} \sum_{q=0}^{2} \beta_q (A_{i+}^{\mathrm{c}} - A_{i-}^{\mathrm{c}})^{n-q}. \tag{21}$$

In the following we discuss all the above steps in more detail, with emphasis placed on the high-order scheme and the time-stepping procedure.

5.1. *Low-order scheme*

The simplest low-order, positivity-preserving scheme is upwind differencing used in almost all previous FCT proposed methods. In our notation for the linear problem we obtain

$$f_{i+} = U_j \bar{\phi}_j^n, \quad U_j \geqslant 0 \tag{22a}$$

$$f_{i-} = U_j \bar{\phi}_j^n, \quad U_j < 0. \tag{22b}$$

For the non-linear problem at elemental interfaces the appropriate sign is determined using the Roe speed,[16] which is an average state between boundary values of adjacent elements. The advancement of the low-order solution therefore proceeds as

$$\bar{\phi}_j^{\mathrm{td}} = \bar{\phi}_j^n - \Delta t \sum_{q=0}^{2} \beta_q \left(\frac{f_{i+}^n - f_{i-}^n}{\Delta x_j} \right)^{n-q}. \tag{23}$$

The transportive–diffusive field $\bar{\phi}_j^{\mathrm{td}}$ is computed at the Gauss–Chebyshev (j) points which are the midpoints (in the transformed θ-space) of the cells.

5.2. *High-order scheme: spectral element method*

To be consistent with the integration scheme in (21) and (23), here we use a third-order Adams–Bashforth time-stepping scheme, i.e.

$$\bar{\phi}_j^{n+1} = \bar{\phi}_j^n - \frac{\Delta t}{\Delta x_j} \sum_{q=0}^{2} \beta_q (F_{i+} - F_{i-})^{n-q}, \tag{24}$$

where β_q are appropriate weight coefficients.[17] The high-order flux $F_i = U_i \phi_i$ is computed at the Gauss–Lobatto–Chebyshev points. A reconstruction operation is then involved to recover point values from the cell-averaged field $\bar{\phi}_j$.

A brief description of the spectral element has been given in Sections 2 and 3. Here we establish the connection between the local (elemental) reference system and the global (physical) co-ordinate system. For the set of Gauss–Lobatto–Chebyshev points the local co-ordinate is given

by

$$r_i^k = -\cos\left(\frac{\pi i}{N}\right), \quad 0 \leqslant i \leqslant N, \tag{25a}$$

which is related to the global co-ordinate x through the equation

$$x = \frac{L^k}{2} r^k + \frac{x_L^k + x_R^k}{2}; \tag{25b}$$

here x_L^k and x_R^k denote the left and right co-ordinates of the elemental boundaries. The interpolant of $\phi(x)$ in the kth element is then represented as

$$\phi^k(r) = \sum_{i=0}^{N} h_i(r^k)\phi_i^k. \tag{26}$$

Here ϕ_i^k are nodal values of ϕ and h_i are shape functions corresponding to element k and node i, with the property $h_i(r_j^k) = \delta_{ij}$, where δ_{ij} is the Kronecker delta symbol (equation (9a)). Expressions of these Lagrangian interpolants (as well as their derivatives) in terms of Chebyshev or Legendre polynomials can be found in Reference 15.

5.3. *Flux limiter–filter*

A key component of a successful FCT algorithm is the flux limiter employed, since it conveys an appropriate amount of dissipation from the low- to high-order scheme so that monotonicity is preserved and undesirable overshoots are avoided. Experimentation with the proposed limiters in References 6, 8 and 11 reveals some noticeable differences. Here we have chosen to use a simple limiter based on the original ideas of Boris and Book[6] and the extensions presented in Reference 11. A modification introduced here is the incorporation of a variable cell size Δx_j. A complete description of our limiter is as follows:

$$\begin{aligned} &s_1 = \operatorname{sign}(A_{i+}), \qquad s_2 = \operatorname{sign}(\bar{\phi}_{j+1}^{td} - \bar{\phi}_j^{td}), \qquad s_3 = \tfrac{1}{2}(s_1 + s_2), \\ &a_1 = s_1(\bar{\phi}_{j+2}^{td} - \bar{\phi}_{j+1}^{td})\Delta x_j, \qquad a_2 = s_1(\bar{\phi}_j^{td} - \bar{\phi}_{j-1}^{td})\Delta x_j, \\ &a_3 = s_1 \max[0, \min[s_3 A_{i+}\Delta t, a_1, a_2]], \qquad A_{i+}^c = a_3/\Delta t. \end{aligned} \tag{27}$$

The filter used in some of the computations is a pth-order filter developed by Vandeven[4] and given by

$$\sigma_p(x) = 1 - \frac{(2p-1)!}{[(p-1)!]^2} \int_0^x [t(1-t)]^{p-1} \mathrm{d}t. \tag{28}$$

While this filter is very similar to the classical raised cosine and sharpened raised cosine for $p = 3$ and 8 respectively, it has been shown in Reference 4 that a prespecified accuracy (controlled directly by the filter order p) can be recovered away from the discontinuity.

6. NUMERICAL EXPERIMENTS

The Vandeven filter has been very effective in recovering spectral-type accuracy for several test cases we have tested in approximating discontinuous functions; however, its use in the discretization of the time-dependent equation (1) gives no improvement at all. To demonstrate this, we plot in Figure 4 the results of a spectral element (collocation) simulation of a square wave linearly

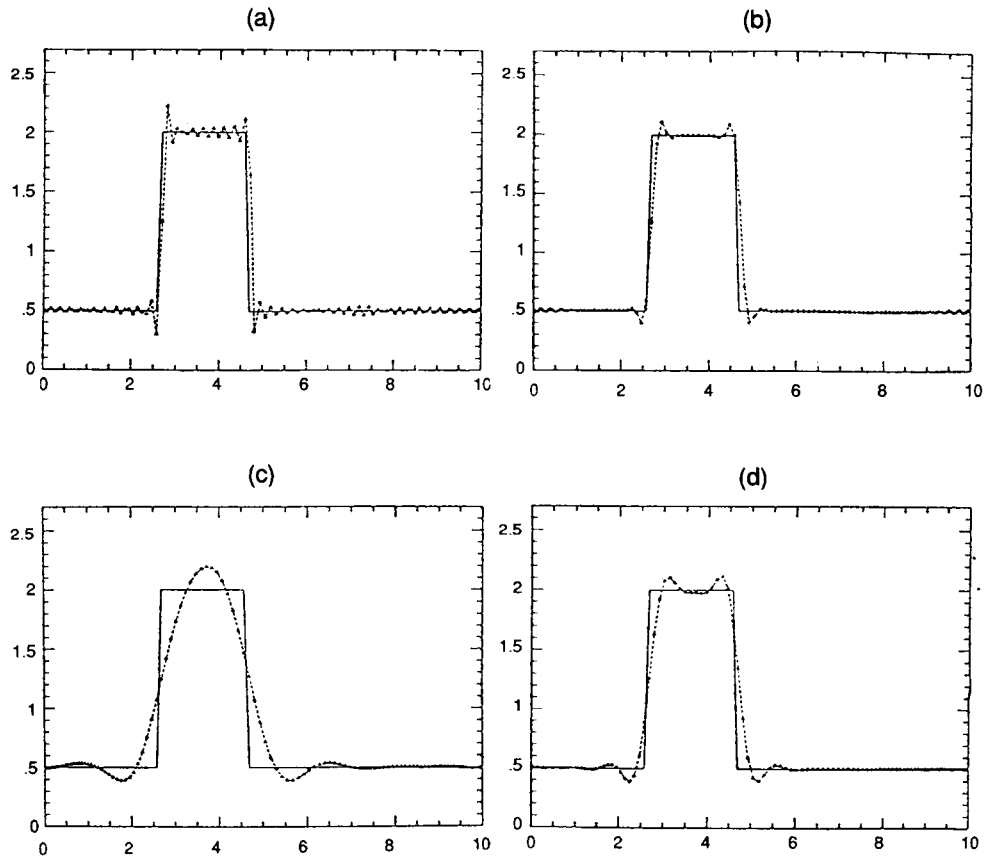

Figure 4. Linear advection of a square wave for (a) an unfiltered solution and (b)–(d) with the Vandeven filter applied: (b) at last time step; (c) every time step; (d) very 100 time steps

advected to the right for various values of the filter order p. The filter is applied here at selected time intervals: at the last time step (Figure 4(b)), every time step (Figure 4(c)) and every 100 time steps (Figure 4(d)). For comparison we also plot the unfiltered solution in Figure 4(a). The results are qualitatively different: in the second case the wave-form is 'smoothed' globally, i.e. deformed essentially, in the other cases major errors are confined around the discontinuities and the boundary points.

6.1. Linear advection

In the following we present results based on the spectral element–FCT algorithm proposed in the previous section. First we simulate the linear advection of a square wave in the periodic interval $x \in [0, 10]$. The wave is located initially between $x = 4{\cdot}0$ and $6{\cdot}0$; after 12 000 time steps it has moved to a new location between $x = 6{\cdot}0$ and $8{\cdot}0$. In Figure 5 we plot the solution for various discretizations: in Figure 5(a) we plot the solution of a Fourier–FCT simulation, in Figure 5(b) the solution of a Chebyshev spectral–FCT discretization (corresponding to a single spectral element) and in Figure 5(c) the solution of a spectral element–FCT discretization corresponding to $K = 2$.

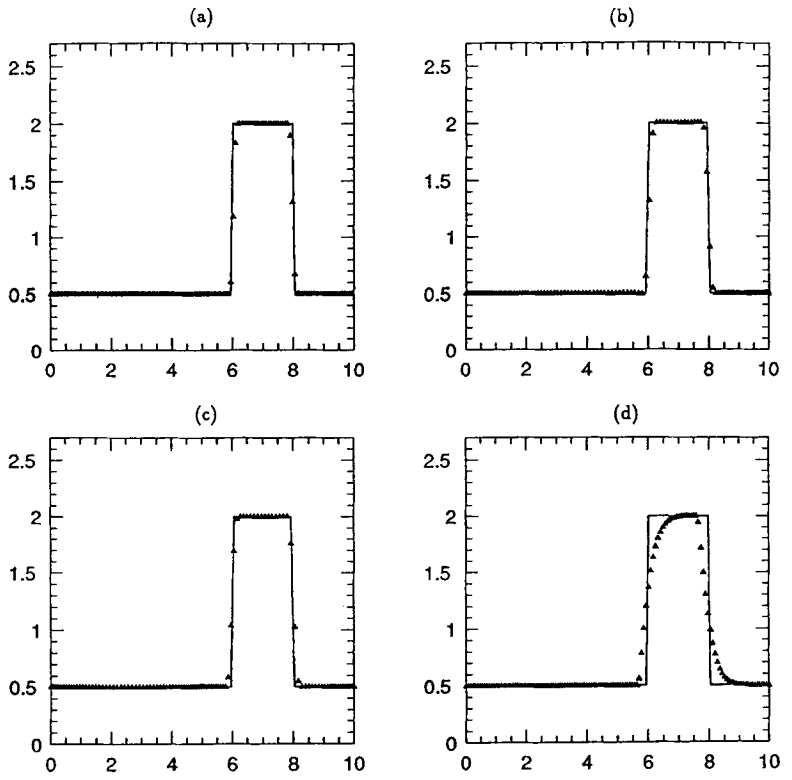

Figure 5. Linear advection of a square wave. The solution is obtained using various FCT schemes: (a) Fourier–FCT; (b) Chebyshev–FCT; (c) spectral element–FCT for $K=2$ elements. The total number of nodes is 128 for all simulations, while the solution is plotted after 12 000 time steps ($\Delta t = 10^{-3}$). In (d) we plot the corresponding solution obtained using a second-order finite difference scheme

Finally, in order to compare the new algorithm with low-order schemes, we plot in Figure 5(d) the solution of a (second-order) finite difference–FCT discretization similar to the one presented in Reference 10. All other simulation parameters are identical for all schemes, including the type of limiter applied and the time step used. From these results it is seen that the spectral–FCT formulation presented in Sections 2 and 3 produces solutions free of oscillations. In addition, the accuracy of the solution is improved dramatically as compared to the finite difference–FCT simulation; the multidomain solution is also comparable to the solution obtained with the Fourier–FCT code.

In the next experiment we compare the linear advection of a combined square wave–semicircle wave-form at different time instances and for similar discretizations as in Figure 5. This problem has also been studied in previous related work[10, 11] and serves as a test for the flux limiter. In particular, here the effect of non-uniform point distribution becomes especially important, since no attempt was made to correct the limiter for such discretizations. Typically, a strong limiter creates a large number of terraces for smoothly varying functions. Initially, the leftmost point of the combined wave-form is located at $x=0{\cdot}5$; the solution is obtained in the periodic domain $x\in[0, 10]$. In Figure 6 we plot the solution after 12 000 time steps for (a) Fourier, (b) $K=1$ and (c) $K=2$ spectral elements. These results should be compared with the solution obtained using

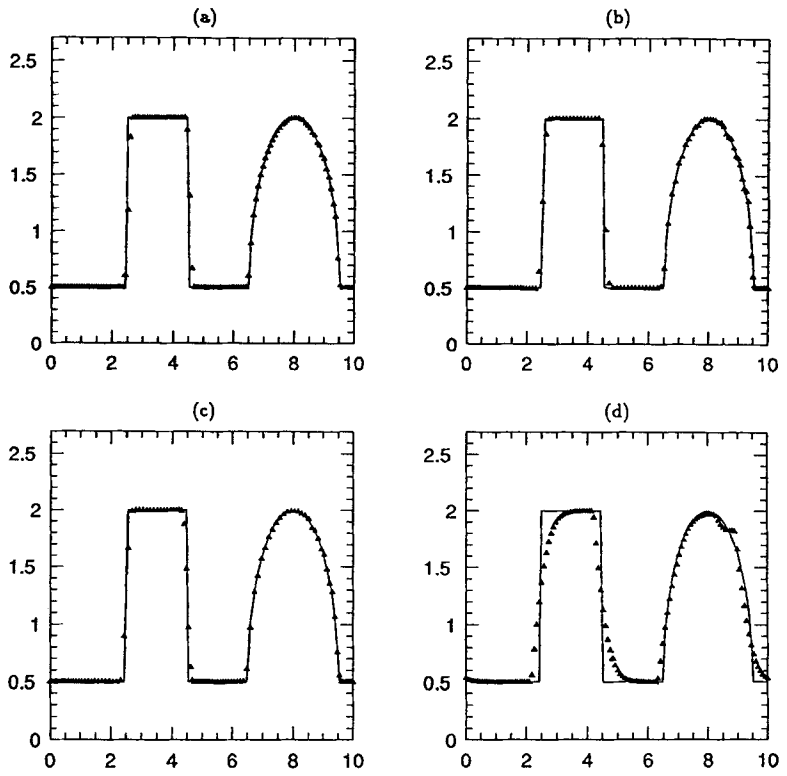

Figure 6. Linear advection of a combined square wave–semicircle. The solution is obtained using various FCT schemes: (a) Fourier–FCT; (b) Chebyshev–FCT; (c) spectral element–FCT for $K = 2$ elements. The total number of nodes is 128 for all simulations, while the solution is plotted after 12 000 time steps ($\Delta t = 10^{-3}$). In (d) we plot the corresponding solution obtained using a second-order finite difference scheme

a second-order finite difference–FCT scheme shown in Figure 6(d). The new feature in this solution is the pronounced terracing effect on the semicircle of the finite difference solution; this effect is less obvious in the spectral solution.

To further investigate the effect of the high-order scheme in creating terraces, we repeat the calculation with the high-order flux computed through an eighth-order formula.[10] In Figures 7(a) and 7(b) we plot the solution obtained after 12 000 time steps using a leapfrog–trapezoidal time-stepping algorithm and a third-order Adams–Basforth scheme respectively. It is interesting to notice that both the square wave and the semicircle are better resolved in the first case; however, the terracing effect is not completely eliminated (Figure 7(a)) and it is certainly more pronounced than in any of the spectral solutions (Figures 6(a)–6(c)). The situation is completely different in Figure 7(b), where the square wave profile is not as sharp as in Figure 7(a) but the terracing effect is completely eliminated. Several other experiments we performed using a high-order finite difference discretization and a third-order Adams–Bashforth time-stepping scheme in advancing both low-order and high-order components of the FCT algorithm gave similar terracing-free results. This is a new finding and leads to the conclusion that non-dispersive high-order time-stepping schemes can completely eliminate the formation of unphysical plateaux in smoothly varying solutions. Unfortunately, the smearing of jump discontinuities is unavoidable with the Adams scheme, as is demonstrated more clearly in Figures 7(c) and 7(d), where we

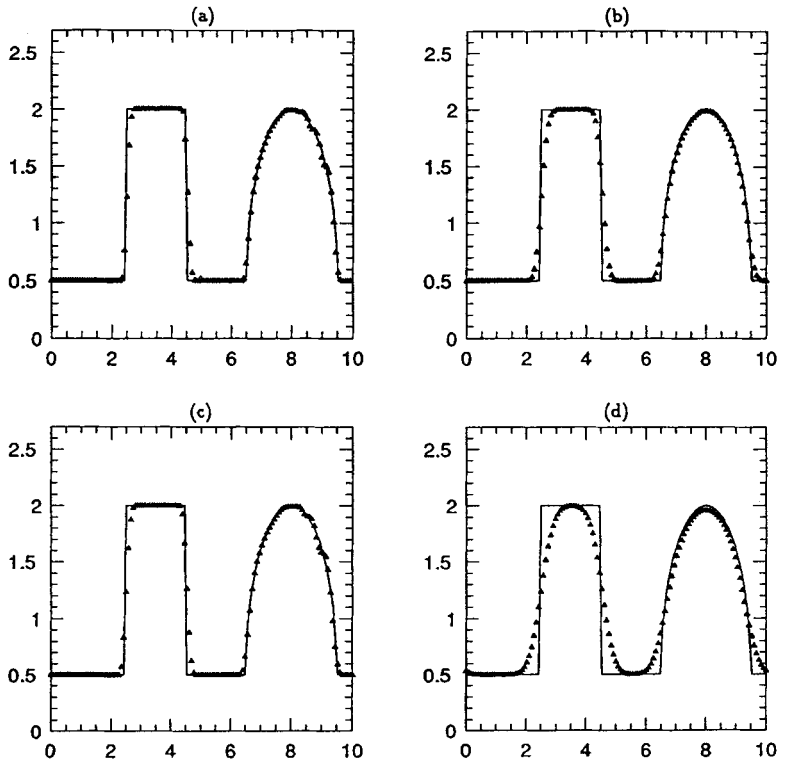

Figure 7. Eighth-order finite difference–FCT solution of the linearly advected combined wave-form (same example as in Figure 6): (a) leapfrog–trapezoidal, 12 000 time steps; (b) Adams–Bashforth third-order, 12 000 time steps; (c) leapfrog–trapezoidal, 52 000 time steps; (d) Adams–Bashforth third-order, 52 000 time steps. The time step is $\Delta t = 10^{-3}$ for all cases

plot the solution corresponding to Figures 7(a) and (7d) after 52 000 time steps. These preliminary results suggest that an ideal time discretization scheme for the problems we examine here will consist of a hybrid or adaptive algorithm that is constructed from both the leapfrog as well as the Adams scheme, which are activated in regions with strong discontinuities and smooth variations respectively.

6.2. Inviscid Burgers equation

In this subsection we present solutions of the inviscid Burgers equation from three experiments corresponding to different initial conditions. First we consider the evolution of an initially *continuous* (parabolic) profile. The profile is steepened after some time and a shock is formed. A similar case was treated in Reference 11 using a Fourier–FCT formulation similar to the one presented in Section 2. The main result of that simulation (which we verified in our work) is that oscillations may develop in the back side of the shock which can be removed by using a high-order filter. Here we are employing the spectral element–FCT formulation to simulate the same case. First a spectral ($K = 1$ element) solution is presented through a series of plots in Figures 8(a)–8(d). The accuracy obtained is comparable to the Fourier–FCT solution with a similar type of odd–even oscillations present in the back side of the shock. On increasing the

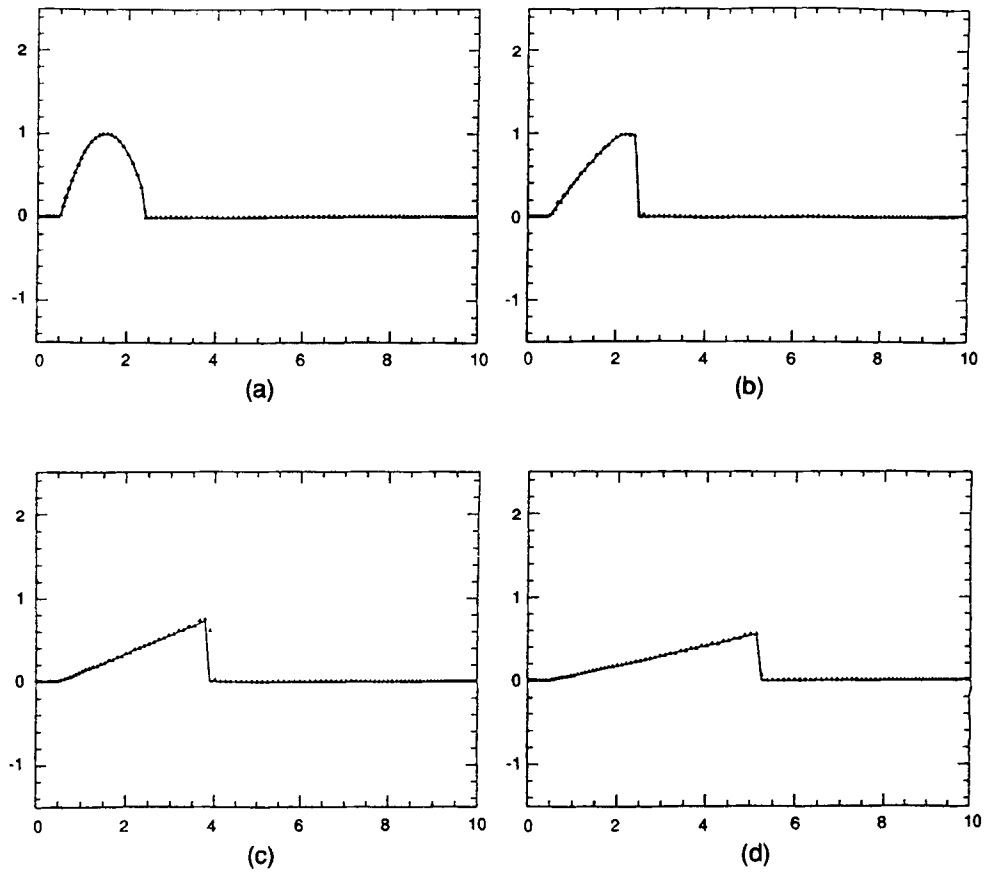

Figure 8. Spectral (Chebyshev) solution of the inviscid Burgers equation using $N = 128$ and $\Delta t = 3{\cdot}9063 \times 10^{-3}$: (a) initial condition; (b) solution after 200 time steps; (c) solution after 1000 time steps; (d) solution after 2000 time steps

number of elements, however, the accuracy of the solution is improved significantly in terms of resolving the discontinuity more accurately as well as removing the aforementioned oscillations without the use of a filter. The solution for a particular discretization ($K = 8$, $N = 16$) is presented in Figures 9(a)–9(d). This type of behaviour is typical for all other spectral element discretizations we tested; oscillations tend to form only for the fewer-element cases.

As a second test case we consider an initial condition corresponding to multiple jump discontinuities as shown in Figure 10(a). The discretization employed corresponds to $K = 10$ elements of 20 Gauss–Lobatto points each, while the time step used is $\Delta t = 10^{-3}$. The solution is plotted in Figure 10 at times (b) $t = 0{\cdot}6$, (c) $t = 1{\cdot}2$, (d) $t = 1{\cdot}8$, (e) $t = 2{\cdot}4$ and (f) $t = 3{\cdot}0$. The solid line correspond to the exact solution and the symbols correspond to the spectral element–FCT solution. There are several features to be noticed in this solution. As far as the shocks are concerned, we observe correct speeds, no overshoots or undershoots and very accurate coalescence. Similarly, the expansion is simulated correctly, free of oscillations or terracing as well as free of overshoots or undershoots at the two corners. To examine the effect of resolution using a coarser mesh, we simulate the same solution using $K = 10$ elements of 11 Gauss–Lobatto points

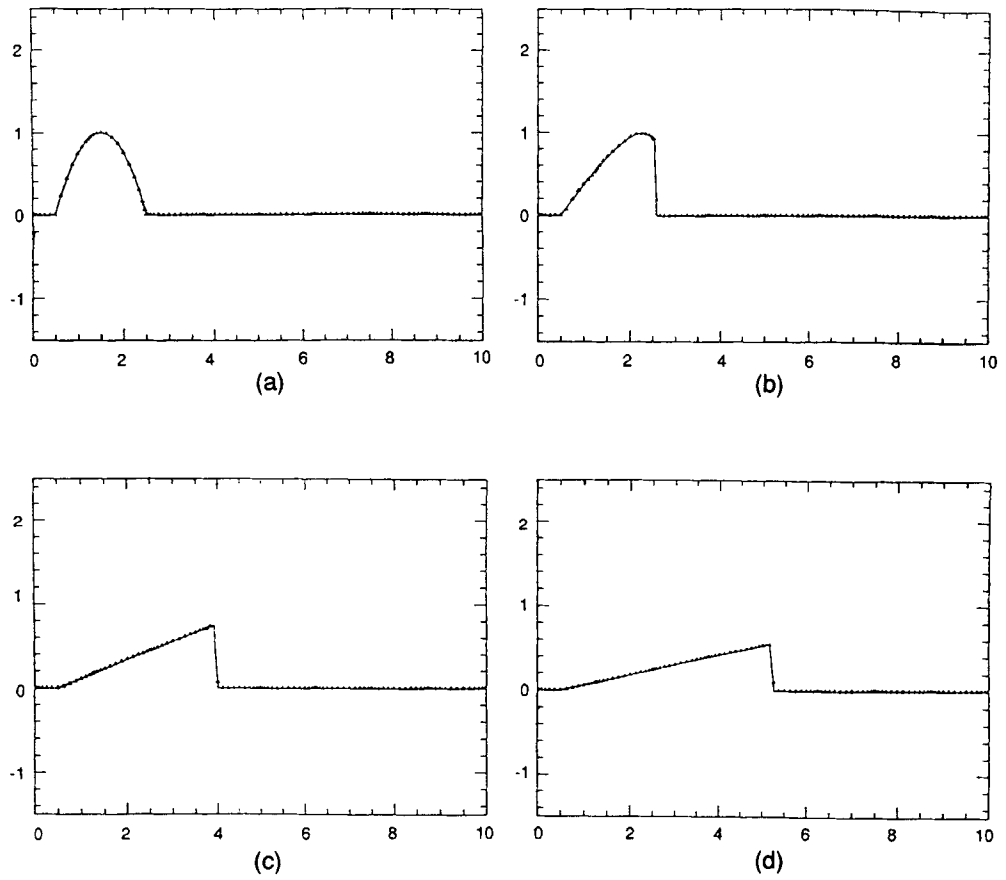

Figure 9. Spectral element solution of the inviscid Burgers equation using $K=8$, $N=16$ and $\Delta t=3{\cdot}9063\times10^{-3}$: (a) initial condition; (b) solution after 200 time steps; (c) solution after 1000 time steps; (d) solution after 2000 time steps

each. The obtained solution is shown in Figures 11(a)–11(f), where again all features of the exact solution are very accurately represented.

As a last example we consider the solution of the inviscid Burgers equation corresponding to the initial condition $u(x, 0)=0{\cdot}3+0{\cdot}7\sin(\pi x)$. In contrast to the previous solutions, this initial condition leads to both left- and right-travelling waves. The matching of the solution at elemental interfaces is upwind, with the appropriate sign determined by a simple Roe averaging procedure[16] of reconstructed boundary values. Unlike the previous examples, here we apply the limiter only in the elements around the shock (see Section 7). The time step used in this simulation is $\Delta t=2\times10^{-4}$. In Figure 12 we plot the solution after a shock has formed at time $t=3{\cdot}0$; this solution is obtained using $K=15$ elements of eight Gauss–Lobatto points each. As shown in the figure, the solution is free of spurious oscillations and the (one-point) shock has the correct speed.

7. DISCUSSION

In this work we have formulated an algorithm based on spectral element discretizations and flux-corrected transport (FCT) concepts. The results presented justify the need for using high-

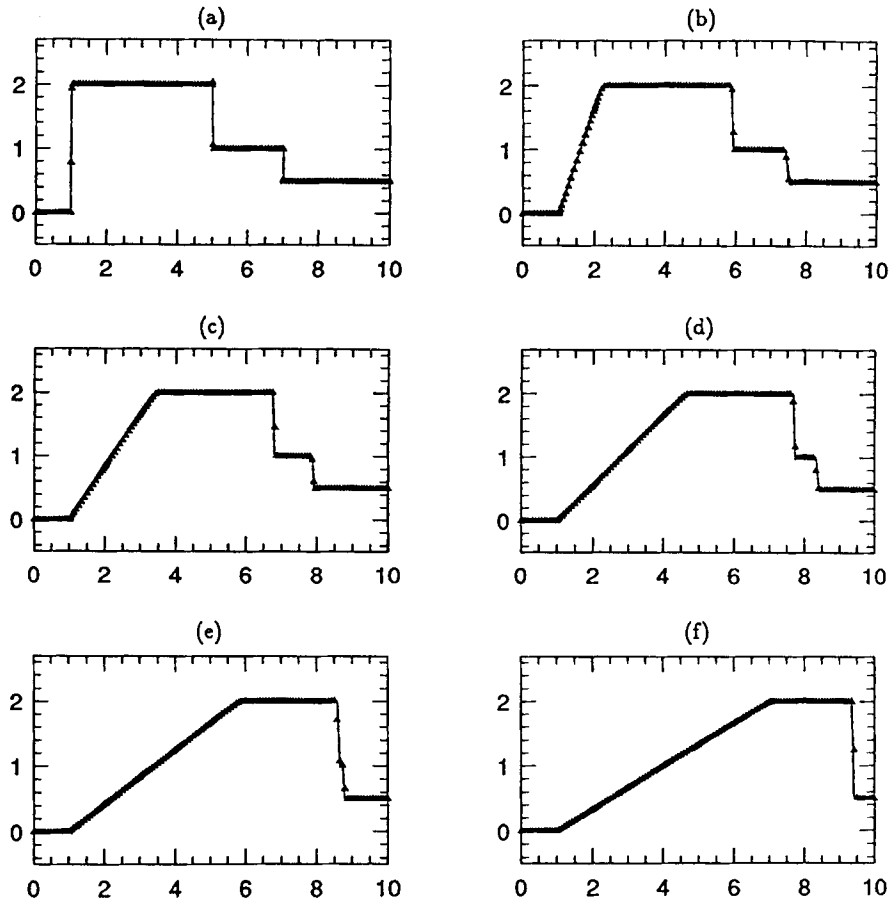

Figure 10. Spectral element solution of the inviscid Burgers equation using $K=10$, $N=20$ and $\Delta t=10^{-3}$: (a) initial condition; (b) solution at $t=0{\cdot}6$; (c) $t=1{\cdot}2$; (d) $t=1{\cdot}8$; (e) $t=2{\cdot}4$; (f) $t=3{\cdot}0$

order schemes to improve the quality of solutions obtained via FCT techniques, in agreement with previous recommendations.[10] We have made no special attempt to devise a flux limiter consistent with non-uniform spectral discretizations; however, we found that the simple limiter of Boris and Book[6] is effective in correcting overshoots or undershoots that may develop during the time evolution of the solution. The question which has never been addressed in any of the previous investigations is if a *spectral accuracy* can be recovered (in the smooth regions of the solution) employing spectral schemes that use FCT ideas. The answer is unfortunately not a simple one and is ultimately related to the effectiveness of the flux limiter. In a smooth region, for example, where the limiter need not be activated ($C_i=1$ in equation (20)), only the high-order (spectral) discretization is employed (see Section 5) and thus high accuracy is expected in that part of the domain. In our experiments, however, we found that for smoothly varying functions (e.g. a semicircle) the limiter employed here is also activated ($C_i<1$) in the smooth region, while in the square wave experiment the limiter is activated only around the two points of discontinuities. The situation is similar with the inviscid Burgers equation. To recover exponential convergence, however, away from the discontinuity we apply the flux limiter *adaptively* on those spectral

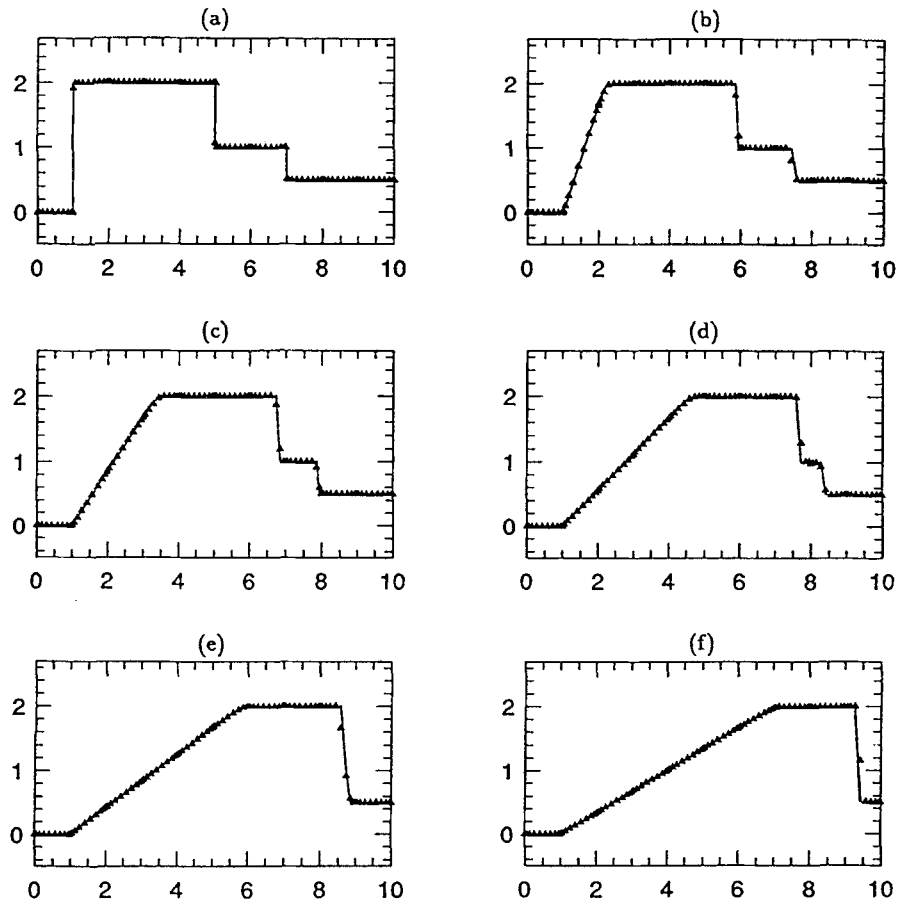

Figure 11. Spectral element solution of the inviscid Burgers equation using $K=10$, $N=11$ and $\Delta t=10^{-3}$: (a) initial condition; (b) solution at $t=0{\cdot}6$; (c) $t=1{\cdot}2$; (d) $t=1{\cdot}8$; (e) $t=2{\cdot}4$; (f) $t=3{\cdot}0$

elements only in which the corresponding spectral expansions converge at a very slow rate, i.e. the element where the shock is located and the two elements adjacent to it. This idea was implemented for the solution of Figure 12 and the pointwise error of the solution at time $t=3{\cdot}0$ is plotted in Figure 13 for two discretizations corresponding to $K=15$ and $N=4$ and 8. We see that indeed as we double the local resolution, keeping the number of elements constant, the error decreases by two orders of magnitude away from the shock, suggestive of spectral-type convergence. Recent progress in developing one-sided filters makes it possible to also recover high accuracy in the region around the shock.[18] Similar results and spectral convergence have been obtained recently using a non-oscillatory reconstruction and spectral element discretization.[19]

The approach of partial adaptive limiting implemented here is essential in recovering spectral convergence in smooth regions. It is quite general and can easily be extended to multishock solutions and systems of hyperbolic laws. There are other issues associated with computational cost and time step restrictions which are typical in spectral-type methods. Here we have only addressed the approximation properties of the new algorithm and demonstrated how the method can potentially be competitive with currently used finite difference techniques by requiring much

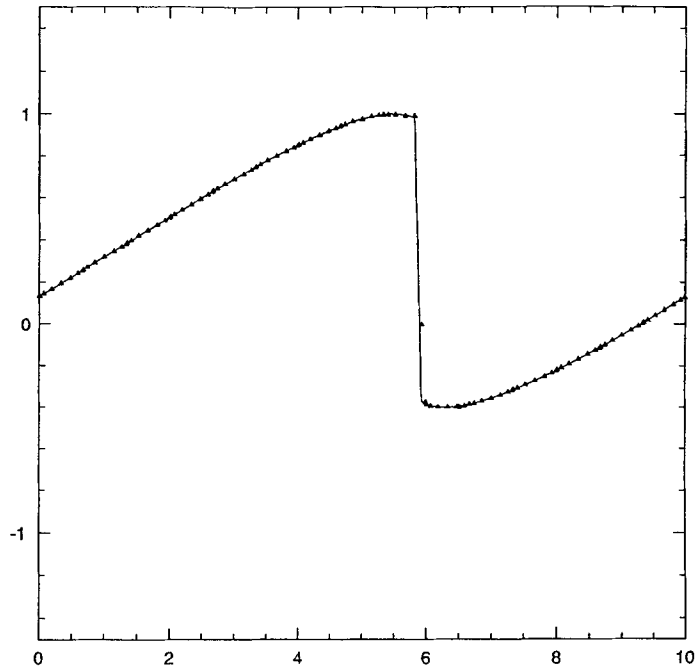

Figure 12. Spectral element solution of the inviscid Burgers equation using $K=15$, $N=8$ and $\Delta t=2\times10^{-4}$. The initial condition is $\phi(x,0)=0{\cdot}3+0{\cdot}7\sin(\pi x)$. The solution is plotted at time $t=3{\cdot}0$

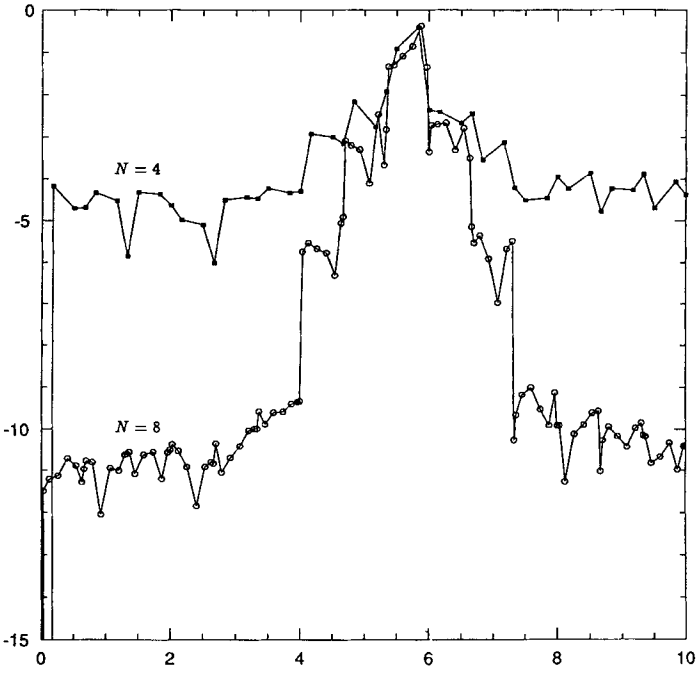

Figure 13. Pointwise logarithmic error of reconstructed values for the solution of Figure 12 for $K=15$ and $N=4$ (squares) and $N=8$ (circles)

less resolution of points (see examples of the Burgers equation). Work in progress addressed the time step restriction by implementing recently developed techniques[20, 21] or resorting to implicit time advancement. We are currently investigating these issues and we will report results in a future publication.

ACKNOWLEDGEMENTS

We would like to thank Professor D. Gottlieb for many helpful suggestions. We would also like to thank Dr. D. Sidilkover for several interesting discussions. This work was supported by AFOSR Grant 90-0261.

REFERENCES

1. A. T. Patera, 'A spectral element method for fluid dynamics; laminar flow in a channel expansions', *J. Comput. Phys.* **54,** 468 (1984).
2. G. E. Karniadakis, E. T. Bullister and A. T. Patera, 'A spectral element method for solution of two- and three-dimensional time dependent Navier–Stokes equations', in *Finite Element Methods for Nonlinear Problems*, Springer, New York, 1985, p. 803.
3. G. E. Karniadakis, 'Spectral element simulations of laminar and turbulent flows in complex geometries', *Appl. Numer. Math.*, **6,** 85 (1989).
4. H. Vandeven, 'Family of spectral filters for discontinuous problems', *Ph.D. Thesis*, CMAP, Ecole Polytechnique, 1989.
5. P. D. Lax, 'Accuracy and resolution in the computation of solutions of linear and nonlinear equations', in *Recent Advances in Numerical Analysis, Proc. Symp. Math. Research Center, University of Wisconsin*, Academic, New York, 1978, p. 107.
6. J. P. Boris and D. L. Book, 'Flux-corrected transport. I SHASTA, a transport algorithm that works', *J. Comput. Phys.*, **11,** 38 (1973).
7. J. P. Boris and D. L. Book, 'Flux-corrected transport. III Minimal-error FCT algorithms', *J. Comput. Phys.*, **10,** 397 (1975).
8. S. T. Zalesak, 'Fully multidimensional flux-corrected algorithm for fluids', *J. Comput. Phys.*, **31,** 335 (1979).
9. S. K. Godunov, 'A finite-difference method for the numerical computation of discontinuous solutions of the equations of fluid dynamics', *Mat. Sb.*, **47,** 271 (1959).
10. S. T. Zalesak, 'Very high order and pseudospectral flux-corrected transport FCT algorithms for conservation laws', *IMACS Symp. on Computational Methods for Partial Differential Equations*, 1981, p. 126.
11. B. E. McDonald, 'Flux-corrected pseudospectral method for scalar hyperbolic conservation laws', *J. Comput. Phys.*, **82,** 413 (1989).
12. E. M. Rønquist, 'Optimal spectral element methods for the unsteady three-dimensional incompressible Navier–Stokes equations', *Ph.D. Thesis*, Massachusetts Institute of Technology, 1988.
13. Y. Maday and A. T. Patera, 'Spectral element methods for the Navier–Stokes equations', *ASME State-of-the-art Surveys in Computational Mechanics*, ASME, New York, 1987.
14. W. Cai, D. Gottlieb and A. Harten, 'Cell averaging Chebyshev methods for hyperbolic problems', *Technical Report 90-27*, ICASE, NASA Langley Research Center, 1990.
15. D. Gottlieb and S. A. Orszag, *Numerical Analysis of Spectral Methods: Theory and Applications*, SIAM, Philadelphia, PA, 1977.
16. P. L. Roe, 'Approximate Riemann solvers, parameter vectors, and difference schemes', *J. Comput. Phys.*, **43,** 357 (1981).
17. C. W. Gear, *Numerical Initial Value Problems in Ordinary Differential Equations*, Prentice-Hall, Englewood Cliffs, NJ, 1973.
18. W. Cai, D. Gottlieb and C. W. Shu, 'On one-sided filters for spectral Fourier approximations of discontinuous functions', *Technical Report*, Brown University, 1991.
19. D. Sidilkover and G. E. Karniadakis, 'Non-oscillatory spectral Chebyshev method for shock wave calculations', *Fifth Conf. on Domain Decomposition Methods for P.D.E.s*, SIAM, Philadelphia, PA, 1991.
20. D. Kosloff and H. Tal-Ezer, 'Modified Chebyshev pseudospectral method with $O(N^{-1})$ time step restriction', *Technical Report 89-71*, ICASE, NASA Langley Research Center, 1989.
21. B. Fornberg, 'An improved pseudospectral method for initial-value problems', *J. Comput. Phys.*, **91,** 381 (1990).